Click Here for Full Article

Upper crustal seismic structure along the Southeast Indian Ridge: Evolution from 0 to 550 ka and variation with axial morphology

Janet M. Baran, Suzanne M. Carbotte, and James R. Cochran
Lamont–Doherty Earth Observatory, Earth Institute at Columbia University, 61 Route 9W, Palisades, New York 10964, USA (carbotte@ldeo.columbia.edu)

Mladen R. Nedimović
Lamont–Doherty Earth Observatory, Earth Institute at Columbia University, 61 Route 9W, Palisades, New York 10964, USA

Also at Department of Earth Sciences, Life Sciences Centre, Dalhousie University, Halifax, Nova Scotia B3H 4J1, Canada

[1] The seismic structure of uppermost crust evolves after crustal formation with precipitation of alteration minerals during ridge-flank hydrothermal circulation. However, key parameters of crustal evolution including depth extent and rates of change in crustal properties, and factors contributing to this evolution remain poorly understood. Here, long-offset multichannel seismic data are used to study the evolution of seismic layer 2A and uppermost 2B from 0 to 550 ka at three segments of the intermediate spreading rate Southeast Indian Ridge. The segments differ in on-axis morphology and structure with crustal magma bodies imaged at axial high and rifted high segments P1 and P2, but not at axial valley segment S1 and marked differences in thermal conditions within the upper crust are inferred. One-dimensional travel time modeling of common midpoint supergathers is used to determine the thickness and velocity of layer 2A and velocity of uppermost 2B. At all three segments, layer 2A velocities are higher in 550 ka crust than on-axis (by 7–14%) with the largest increases at segments P1 and P2. Velocities increase more rapidly (by 125 ka) at P1 with spatial variations in velocity gradients linked to location of the underlying crustal magma body. We attribute these differences in crustal evolution to higher rates of fluid flow and temperatures of reaction at these ridge segments where crustal magma bodies are present. Layer 2A thickens off-axis at segments P1 and P2 but not at S1; both off-axis volcanic thickening and downward propagation of a cracking front linked to the vigor of axial hydrothermal activity could contribute to these differences. In zero-age crust, layer 2B velocities are significantly lower at segments P1 and P2 than S1 (5.0, 5.4, and 5.8 km/s respectively), whereas similar velocities are measured off-axis at all segments (5.7–5.9 km/s). Lower on-axis 2B velocities at segments P1 and P2 can be partly attributed to thinner layer 2A, with lower overburden pressures leading to higher porosities in shallowest 2B. However, other factors must also contribute. Likely candidates include subaxial deformation due to magmatic processes and enhanced cracking with axial hydrothermal activity at these segments with crustal magma bodies.

1. Introduction

[2] Seismic layer 2A is the low velocity uppermost portion of the igneous oceanic crust [e.g., *Houtz and Ewing*, 1976] with compressional wave velocities as low as 2.2–2.5 km/s measured in young crust. Such low velocities are believed to reflect high porosities within the extrusive basalts inherited from volcanic emplacement processes and fracturing [*Purdy*, 1987; *Vera et al.*, 1990; *Christeson et al.*, 1996]. The velocity of layer 2A increases as crust ages away from the spreading axis reaching ∼4.3 km/s in mature crust in ∼10 Ma [*Grevemeyer et al.*, 1999; *Carlson*, 1998]. This increase in velocity is commonly attributed to closure of cracks and volcanic porosity by compaction and to precipitation of hydrothermal products within voids in the extrusive section [e.g., *Jacobson*, 1992; *Grevemeyer and Bartetzko*, 2004]. The geometry of cracks and voids can strongly affect seismic velocities [*Kuster and Toksoz*, 1974; *Toksoz et al.*, 1976; *Wilkens et al.*, 1991]. From their study of velocity-porosity relationships for a range of pore sizes, *Wilkens et al.* [1991] conclude that the observed doubling of seismic layer 2A velocities as crust ages could arise from only a small (5%) reduction in effective porosity through sealing of small thin cracks with hydrothermal precipitates. Hydrothermal circulation within the near axis regime as well as longer-term low temperature fluid circulation within the shallow crust on the ridge flanks may both contribute to layer 2A porosity reduction and therefore the observed velocity increase.

[3] At the base of layer 2A, seismic velocities rapidly increase to values typical of layer 2B (4.5–5.5 km/s) over a depth interval of a few to several hundred meters. This steep gradient gives rise to a refracted arrival that can be detected by Multichannel seismic (MCS) surveys conducted with a long hydrophone streamer (greater than 2 km) [e.g., *Harding et al.*, 1993; *Vera and Diebold*, 1994]. In MCS studies carried out within a number of ridge axis regions since the late 1980s, this arrival has been successfully stacked and mapped, providing constraints on 2A structure at different spreading rates. These studies reveal a thin layer 2A, 100–200 m thick, along the axis of fast spreading ridges, doubling to tripling in thickness within ∼5 km of the ridge axis [e.g., *Vera and Diebold*, 1994; *Kent et al.*, 1994; *Hooft et al.*, 1996; *Carbotte et al.*, 1997, 2000; *Hussenoeder et al.*, 2002a]. In contrast, layer 2A is thicker along the axis of slow spreading ridges (400–600 m) with minor to no thickening away from the axis [*Hussenoeder et al.*, 2002b; *Singh et al.*, 2006]. Recent studies at intermediate spreading ridges show segment to segment variations in layer 2A thickness which suggest that both axial morphology and lava composition are linked to layer 2A structure, in addition to spreading rate [*Blacic et al.*, 2004; *Canales et al.*, 2005; *Van Ark et al.*, 2007; *Jacobs et al.*, 2007]. In a few locations, seismic refraction and MCS data have been used to study changes in layer 2A velocities within the near-axis region. A rapid increase in velocities within ∼100–500 ka of crustal formation is inferred from studies at the fast spreading East Pacific Rise (EPR) [*Hussenoeder et al.*, 2002a; *Grevemeyer and Weigel*, 1997]. Studies at the Mid Atlantic Ridge (MAR) indicate lower rates of 2A velocity increase with crustal aging although the temporal resolution of these studies is inadequate to resolve changes on time scales less than ∼1 myr [*Purdy*, 1987; *Hussenoeder et al.*, 2002b].

[4] The geologic significance of these observations is subject to debate centering on two primary hypotheses for the origin of the high velocity gradient at the base of layer 2A. The first hypothesis suggests that the layer 2A/2B boundary corresponds with the lithologic transition between the extrusive and dike layers of the oceanic crust. Studies of exposed crustal sections [e.g., *Francheteau et al.*, 1990; *Juteau et al.*, 1995; *Karson et al.*, 2002a, 2002b; *Stewart et al.*, 2002] as well as of ophiolites [e.g., *Nicolas*, 1989] show that the upper

part of the oceanic crust is composed of a basaltic extrusive layer, underlain by a transitional layer composed of a mixture of extrusives and dikes, underlain by basaltic dikes. The porosity of the extrusive and dike sections, which directly affect seismic velocity, are expected to be significantly different due to greater fracture density and volume of void space. The porosity contrast between these layers could account for the observed seismic layer 2A arrival. Numerous studies have favored the lithologic interpretation for the 2A/2B transition zone and variations in layer 2A thickness have been most commonly attributed to volcanic emplacement processes [e.g., *Harding et al.*, 1993; *Kent et al.*, 1994; *Vera and Diebold*, 1994; *Christeson et al.*, 1996; *Hooft et al.*, 1996; *Carbotte et al.*, 1997; *Hussenoeder et al.*, 2002a; *Canales et al.*, 2005; *Van Ark et al.*, 2007].

[5] The competing hypothesis is that the base of seismic layer 2A is a porosity boundary within the extrusive layer due to cracking or alteration [*McClain et al.*, 1985; *Becker et al.*, 1989; *Wilcock et al.*, 1992]. The primary evidence supporting this interpretation are observations from DSDP/ODP Hole 504B where an increase in seismic velocity is observed coincident with a decrease in bulk porosity within the extrusive section [*Becker et al.*, 1989]. Recently, *Christeson et al.* [2007] have proposed that the seismic layer 2A/2B boundary is an alteration front, which may be within either the extrusives or dikes. From comparison of MCS observations of layer 2A with mapped lithological data, *Christeson et al.* [2007] find that the layer 2A/2B boundary is located close to or within the dike/extrusive transition zone at Hess Deep, whereas it is found within the extrusive layer at the Blanco escarpment. *Christeson et al.* [2007] suggest that, below the alteration front, cracks heal through hydrothermal metamorphism, infilling by secondary mineralization, and crack closure. It is important to note that the layer 2A/2B transition may coincide with both a lithologic boundary and alteration front, particularly at young ages. Strong gradients in crustal properties associated with the lava/dike transition zone are likely to play an important role in fluid flow in the crust. Indeed, extensive alteration of the dike/lava transition zone is observed within ophiolites [*Johnson and Pariso*, 1987] and in situ crust at DSDP/ODP hole 504B [*Alt et al.*, 1986]. Furthermore, thinner layer 2A in regions of more altered crust is evident in some data sets [e.g., *Nedimović et al.*, 2008] and indicates that contrasts in crustal properties associated with the seismic layer 2A/2B boundary can

migrate within the crust with crustal alteration and aging.

[6] In 2001–2002, an MCS investigation of on- and off-axis crustal structure along the Southeast Indian Ridge (SEIR) was conducted from the *R/V Maurice Ewing* [*Baran et al.*, 2005]. Spreading rates are approximately constant along the SEIR but large changes in axial morphology are observed which have been attributed to gradients in mantle temperature, and hence magma supply to the crust, toward the Australian-Antarctic Discordance Zone. The primary goal of our study was to assess whether differences in crustal structure are associated with these changes in axial morphology. In a previous study, along axis MCS data were used to determine zero-age crustal structure (layer 2A, and the presence, depth, and width of the crustal magma lens) within six segments of contrasting morphology [*Baran et al.*, 2005]. These data indicate that changes in ridge crest morphology are directly linked to the presence or absence of a midcrustal magma body and presumably reflect the impact of crustal magma bodies on the thermal and hence rheological structure of the crust. In this paper, cross-axis changes in the thickness and velocity structure of layer 2A and shallowest 2B within three of these segments are examined. Our analysis is based primarily on one-dimensional modeling of travel time arrivals from closely spaced CMP supergathers (minimum spacing 0.6 km) along a series of axis-parallel and perpendicular MCS profiles. The seismic structure obtained from velocity modeling is compared with coincident seismic reflection images. Our aim is to characterize the evolution of the upper crust as a function of differences in axial morphology and as the crust ages out to 550 ka.

2. Background on the SEIR

[7] The SEIR is an intermediate spreading rate ridge that forms the boundary between the Australian and Antarctic plates. Our study area extends from 47°S, 100°E to 50°S, 111°E, (Figure 1). Seafloor spreading rates are nearly constant within this region at 72 mm/yr [*DeMets et al.*, 1994]. Axial morphology changes along the SEIR from an axial high in the west to an axial valley in the east [*Small and Sandwell*, 1989; *Small*, 1994; *Ma and Cochran*, 1996; *Cochran et al.*, 1997; *Sempere et al.*, 1997] approaching the Australian-Antarctic Discordance (AAD), an area of cold asthenosphere [*Weissel and Hayes*, 1974; *Forsyth et al.*, 1987; *Klein et al.*, 1988; *West et al.*, 1994, 1997].
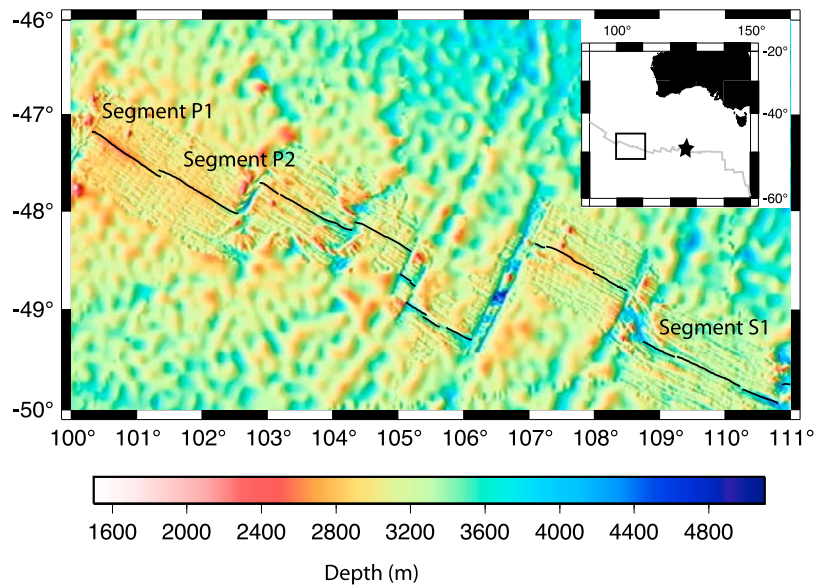
Figure 1. Shaded relief bathymetric map showing the investigated segments of the SEIR. The axis at segment P1 is characterized by a well-developed axial high, whereas segment P2 has a rifted axial high and segment S1 has a shallow axial valley. Segments between P1 and S1 are characterized by a transitional morphology or shallow axial valley. Inset shows the location of our study area southeast of Australia. Black star indicates location of the Australian-Antarctic Discordance.

Changes in magma supply to the ridge axis resulting from variations in mantle temperature are believed to cause the changes in axial morphology along the ridge [Cochran et al., 1997; Sempere et al., 1997; Baran et al., 2005]. Recent seismic refraction results [Holmes et al., 2008] indicate a 1.5 km eastward decrease in crustal thickness from 100° to 116°, consistent with a 30°C decrease in mantle temperature toward the AAD.

[8] Here we focus on three segments, which encompass the range of axial morphology observed along the SEIR:

[9] Segment P1, the westernmost segment, is characterized by a well-defined 15–20 km wide axial high that rises 400 m above surrounding seafloor (Figures 1 and 2a). Along the axis of this segment, average layer 2A thickness is 210 ms two-way travel time (twtt) (~310 m assuming a constant velocity of 3 km/s) and a magma lens is detected under 30% of the segment at an average travel time of 630 ms below the seafloor (~1480 m crustal depth, assuming layer 2B velocity of 5.5 km/s for depth conversion) [Baran et al., 2005].

[10] Segment P2, with a 200 m high and 15–20 km wide rifted axial high, is located immediately to the east of segment P1 (Figures 1 and 2b). This segment is characterized by near-axis inward facing faults, typically located within 1 km of the

ridge axis, with offsets of 50–100 m. Along the axis, the average thickness of layer 2A is 310 ms twtt (~460 m) and a magma lens is imaged under 20% of the segment at an average travel time of 880 ms below the seafloor (~2100 m crustal depth) [Baran et al., 2005].

[11] Segment S1, the easternmost segment, is characterized by a shallow axial valley that is 10–15 km wide and 500–800 m deep (Figures 1 and 2c). Average layer 2A thickness is 530 ms twtt (~800 m) and no magma lens is imaged [Baran et al., 2005].

[12] The differences in on-axis seismic structure observed at the three segments are closely linked to axial morphology. Each morphological type is associated with distinct layer 2A and magma lens characteristics. Changes in axial morphology and shallow crustal structure (layer 2A thickness and magma lens depth) are abrupt along the SEIR [Baran et al., 2005] and are attributed to the threshold response of ridge axis structure to small changes in magma supply from the mantle. Crustal thickness (a common proxy for magma supply) varies from 6.1 km at segment P1, to 5.9 km at P2, with the lowest values of 5.2 km at S1, confirming reduced magma supply at the axial valley segment [Holmes et al., 2008]. With magma bodies imaged at 1.5 and 2.1 km in the crust at segments P1 and P2, higher temperatures are expected in the mid
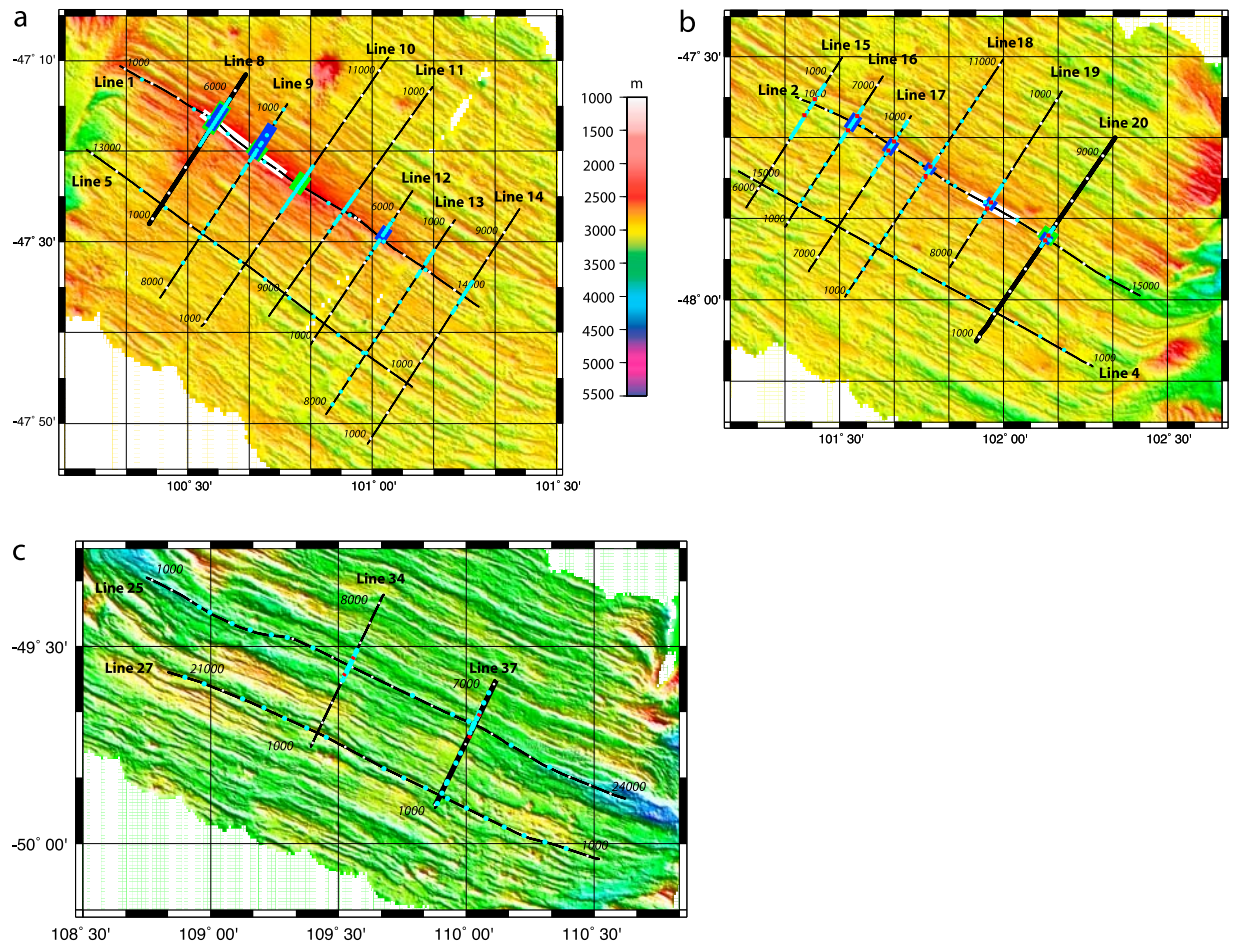
Figure 2. MCS profile locations (black lines) superimposed on bathymetric maps for each ridge segment: (a) segment P1, (b) segment P2, and (c) segment S1. Color scale included in Figure 2a is used for all maps. White dots along lines correspond with every 1000 CMPs. CMPs where velocity modeling was done are indicated with cyan colored dots. Bold black lines are MCS profiles shown in Figure 3. White lines indicate where a magma lens is imaged on along-axis profiles. Green bars delineate the width of the zone of near-axis increase in layer 2A velocity. Blue bars indicate the width of the zone of layer 2A thickening away from the axis. Red diamonds mark the locations of the first inward facing faults defining the shallow axial rift at segment P2 and the deeper wider rift at S1.

crust at these segments than at segment S1, with the warmest temperatures expected at P1.

3. Methods

[13] MCS data were collected along a series of on- and off-axis lines within ridge segments P1, P2, and S1 to determine the characteristics of layer 2A at these segments of varying ridge axis morphology (Figure 2). Several cross-axis MCS lines (from 2 to 7) extending from the ridge axis to 50 km off axis were obtained in each segment. In addition, data were acquired along one axis-parallel line located ~20 km (~550 ka) away from the ridge axis in each segment.

[14] Seismic reflection data were obtained using a 6 km long digital hydrophone streamer with 480

channels and a group spacing of 12.5 m. The seismic source was a tuned 10-gun, 3050 in³ array that was towed at a depth of 8 m. Data were recorded at 2 ms sample rate for 12 s. A nominal shot interval of 50 m was used for the surveys of segments P1, and P2 and a 37.5 m shot interval was used in segment S1. The recorded signal has a bandwidth of 2–100 Hz with dominant frequency in the range of 10–40 Hz. The nominal CMP spacing is 6.25 m, and the data trace fold is 60 for segments P1, and P2, and 80 for segment S1.

3.1. Reflection Sections

[15] Seismic reflection data were processed using Landmark's ProMAX seismic processing package. Band-pass (2–7—100–125 Hz) and f-k filters on shot gathers were applied to remove cable noise

and improve the signal-to-noise ratio. The data traces were then amplitude balanced, edited, and sorted into CMP gathers. This was followed by velocity analysis, normal move out (NMO) correction, stacking, and time domain f-k migration. Optimal stacking velocities for the layer 2A event were chosen from band-pass filtered (2–7—40–60 Hz) constant velocity stacks confined to the mid-offset traces (2–4 km), along with examination of individual CMP gathers. The layer 2A event can typically be well imaged at a range of velocities; we chose the lowest velocities that optimize the 2A image. A composite constant velocity stack that best images the 2A event along the length of the profile was constructed. This stacked section was then f-k migrated and coherency filtered. A 60 ms window encompassing the 2A event was extracted from the migrated 2A section and merged into the main migrated section. Final migrated sections for representative cross-axis lines from each segment are included in Figure 3, showing the layer 2A arrival and magma lens event where present. From the migrated sections, two-way travel time to the layer 2A event is digitized along with the magma lens event. Uncertainties in travel times for these events are ±40 ms and ±30 ms respectively and arise from picking errors and uncertainties in stacking velocities, which are larger for 2A. For more details on the reflection data processing approach taken see *Baran et al.* [2005].

3.2. Velocity Modeling of CMP Supergathers

[16] To ascertain the thickness of layer 2A, constraints are needed on the velocity structure of this layer. We obtain this information by one-dimensional (1-D) travel time modeling of selected CMP gathers. To enhance the 2A arrival for modeling, CMP supergathers were constructed from stacking groups of 10 adjacent CMPs. For axis-parallel lines (0 ka and 550 ka), CMP supergathers were constructed with a spacing of every 1000 CMPs (~6km). In order to constrain changes in layer 2A thickness and velocity within the near-axis region, we chose a closer supergather spacing (every 100 CMPs, or ~0.6 km) for the inner ~6 km wide zone centered on the ridge axis. Beyond the near-axis region, a coarser CMP supergather spacing was chosen (every 500 CMPs, or ~3 km). From this collection of CMP supergathers, a subset with the clearest arrivals (see below) were chosen for traveltime modeling. Modeling was carried out using the JDSeis software package (approach is

described by *Nedimović et al.* [2008]), which enables iterative modeling of reflection and refraction traveltime arrivals for constant velocity and linear velocity gradient layers.

[17] Previous studies indicate that the velocity structure of layer 2A includes an uppermost zone of low velocity with minor changes in velocity with depth underlain by a steep gradient zone where velocity rapidly increases to values typical of layer 2B [*Vera et al.*, 1990; *Harding et al.*, 1993; *Christeson et al.*, 1996; *Blacic et al.*, 2004; *Van Ark et al.*, 2007]. Our starting velocity model was based on this two-part velocity structure, which we refer to as layer $2A_{upper}$ and layer $2A_{lower}$ (also referred to in some studies as the 2A/2B boundary zone). We modeled travel time arrivals for each supergather, including the seafloor reflection, the layer 2B refraction, the layer 2A retrograde refraction, and 2A prograde refraction branch (if present) (Figure 4). In many cases the 2A retrograde branch can be identified only at the triplication with the 2B refraction. A prograde refraction from layer 2A is identified intermittently in off-axis gathers where velocities within layer $2A_{upper}$ are sufficiently high and gradients low that this arrival emerges from the seafloor event within the offset range of the data (Figures 4f, 5b, 5d, 5f, 5h, 5j, 5l, and 6). In the on- and near-axis region, a layer 2A prograde refraction is rarely detected. The thickness and velocity of layer $2A_{upper}$ is constrained by the twtt and offset range of the 2A/2B triplication and the layer 2A prograde refraction event (if present). Constraints on layer $2A_{lower}$ are provided by the triplication, the layer 2A retrograde refraction branch, and layer 2B refraction (Figures 4–6).

[18] CMP supergathers selected for modeling have at minimum a discernable triplication and layer 2B refraction. Figures 7 and 8 show the results of traveltime modeling of layer 2A structure for each of the three segments for the on-axis, axis-parallel, and cross-axis lines. Seafloor topography affects seismic arrival travel times and can limit the validity of the results obtained by 1D modeling in areas of significant bathymetric change. As topographic variations are subdued in the ridge axis parallel direction, results from the axis-parallel transects are considered of highest quality in our analysis and are used to define the primary results of this study. For both axis-parallel and cross-axis lines we distinguish models of higher confidence (large stars in Figures 7 and 8) derived from CMP supergathers with the clearest arrivals from those with less well-defined arrivals (small stars).
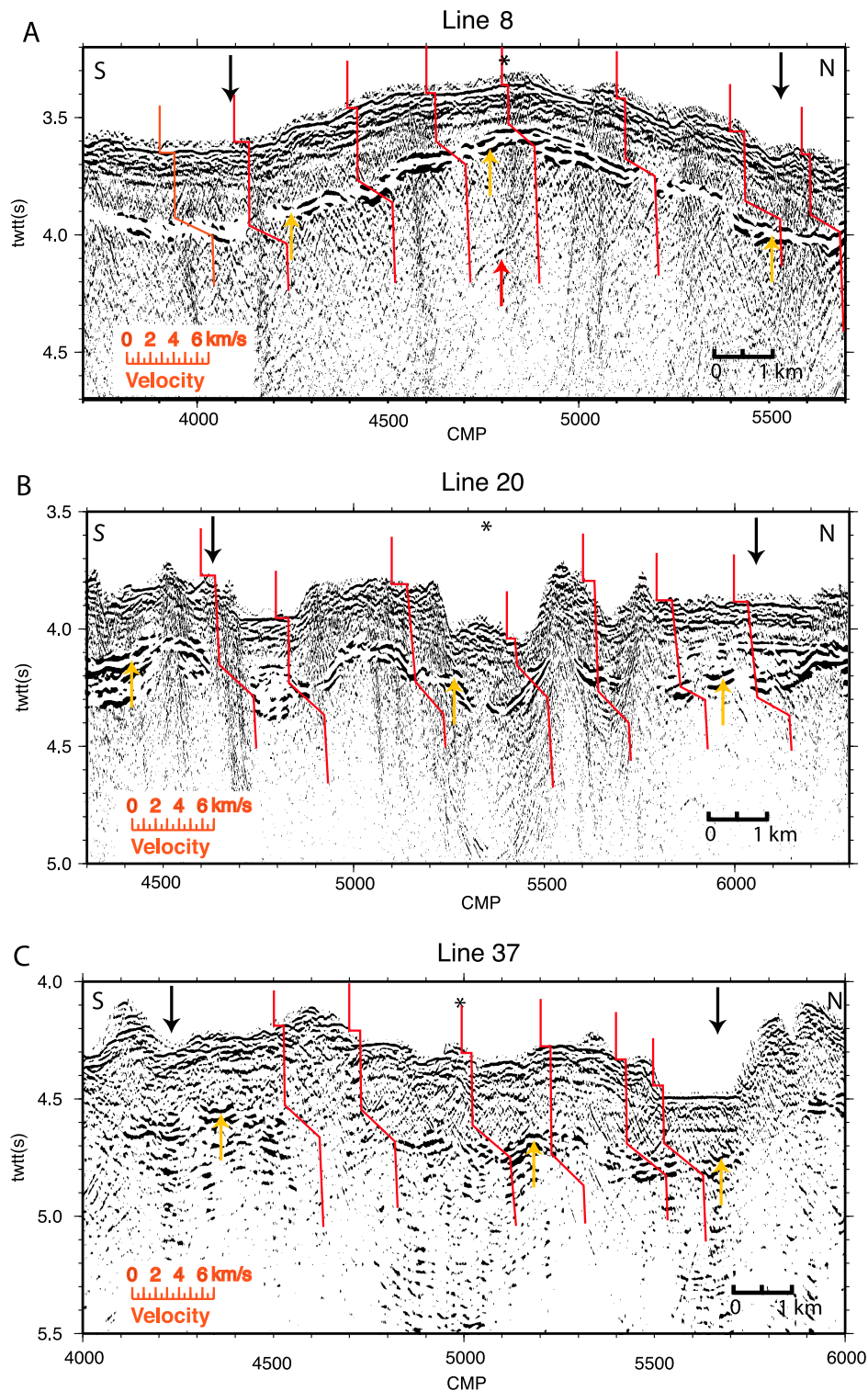
Figure 3. Representative seismic sections across the axis of the three SEIR segments studied: (a) line 8 from segment P1, showing the magma lens reflection beneath the ridge axis and the layer 2A event; (b) line 20 from segment P2; and (c) line 37 from segment S1. The base of the layer 2A event is noted with orange arrows, and the magma lens, where present, is noted with a red arrow. Example velocity-twtt profiles obtained from forward modeling of CMP gathers along each profile are superimposed in red (velocity scale shown in bottom left corner). Profiles are aligned with water column velocity (1.48 km/s) at CMP number of model. Asterisks mark the location of the ridge axis. Black vertical arrows mark the reference location at 4.5 km from the axis (125 ka crust) where off-axis layer 2A velocity and thickness are measured (see section 3.2).
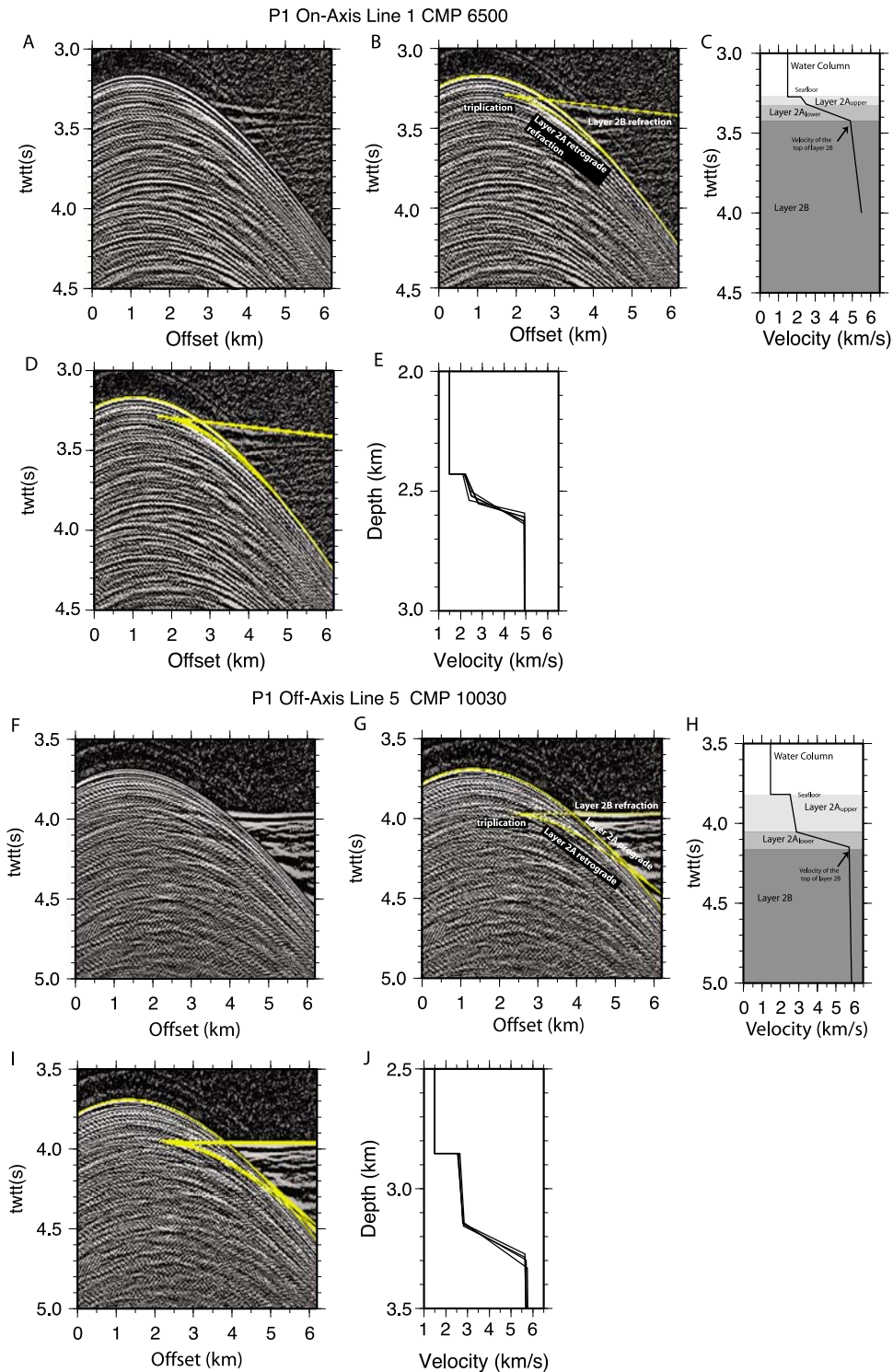
Figure 4. Example traveltime modeling and model error estimation shown for an on-axis and off-axis CMP supergather from segment P1. (a) CMP supergather 6500 from on-axis line 1, displayed with a reducing velocity of 5800 m/s. (b) Same gather with best fit reflection and refraction arrivals determined from 1D ray trace modeling superimposed in yellow and labeled. (c) Corresponding velocity-twtt model. (d) Same CMP supergather with range of acceptable velocity models plotted in yellow. (e) Corresponding velocity models plotted as a function of depth below seafloor. (f–j) Same as Figures 4a–4e but for off-axis supergather CMP 10030 from off-axis line 5.
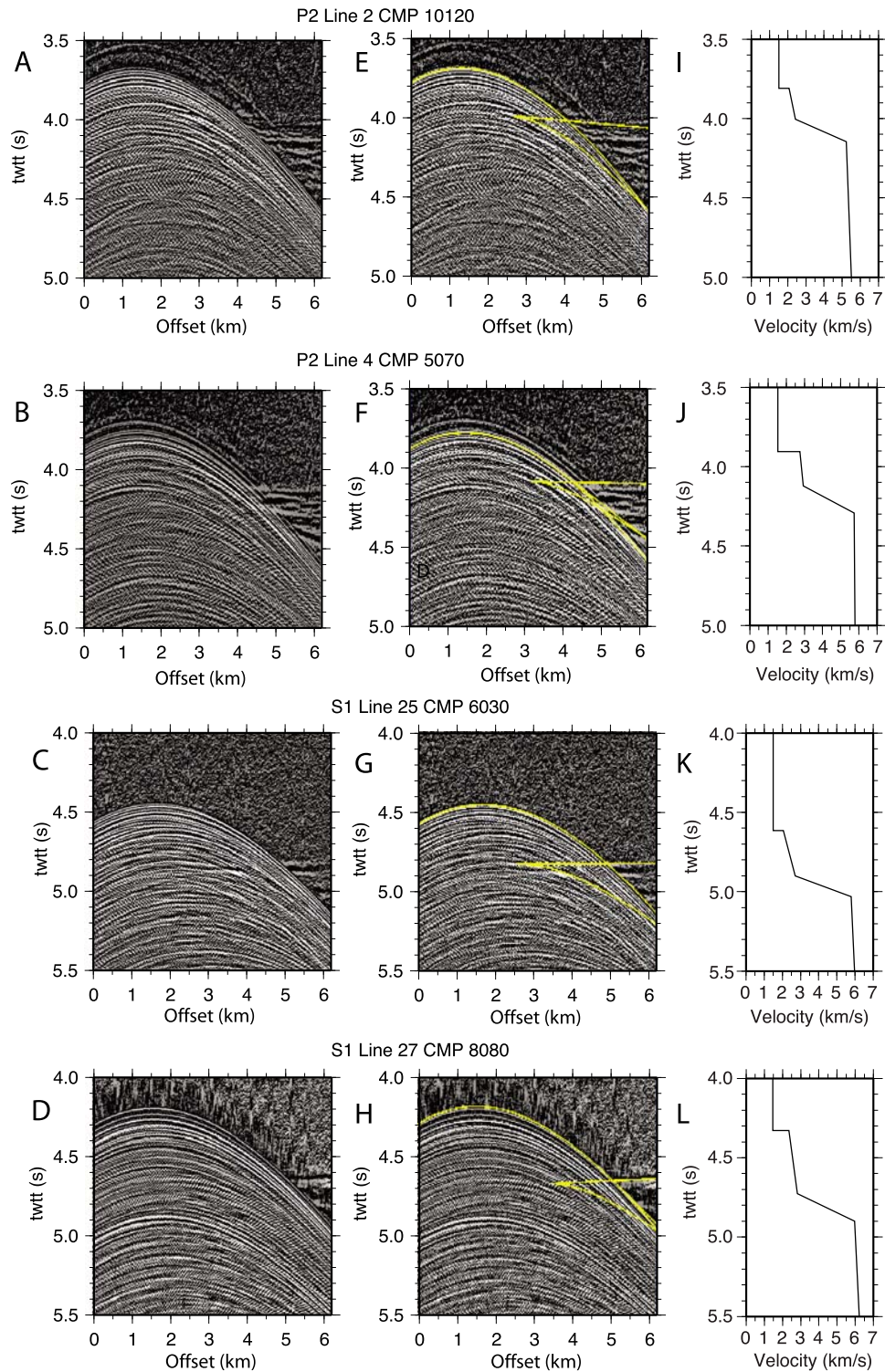
Figure 5. Representative on-axis and off-axis CMP supergathers and traveltime model results for segments P2 and S1 from along-axis profiles. (a–d) Moved out gather (reducing velocity of 5800 m/s), (e–h) gather with model arrivals superimposed in yellow, and (i–l) corresponding velocity model. Figures 5a, 5e, and 5i are for segment P2, CMP 10120 from on-axis Line 2. Figures 5b, 5f, and 5j are for segment P2, CMP 5070 from off-axis Line 4. Figures 5c, 5g, and 5k are for segment S1, CMP 6030 from on-axis Line 25. Figures 5d, 5h, and 5l are for segment S1, CMP 8080 from off-axis line 27.

P1 Line11 CMP 5100
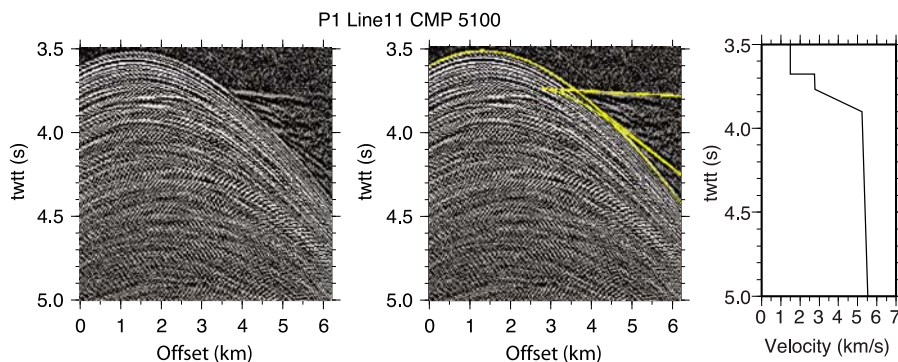
Figure 6. Example of CMP supergather and traveltime model results from cross-axis data. CMP 5120 from profile 11, segment P1. (left) Moved out gather (reducing velocity of 5800 m/s), (middle) gather with model arrivals superimposed in yellow, and (right) corresponding velocity model.

[19] Model solutions are nonunique and a range of models can be found for each CMP supergather, which fit equally well. We estimate uncertainties for our model solutions by determining a range of possible models for six selected CMP supergathers (three on axis and three off axis, e.g., Figure 4). Uncertainties estimated from this analysis are ±0.2 km/s and ±40 m for off-axis velocities and 2A thickness. Model uncertainties are higher (±0.3 km/s and ±60 m for velocity and thickness respectively) for the on-axis data where a 2A prograde event typically does not emerge from the seafloor reflection and model constraints are poorer. Somewhat lower uncertainties were estimated from similar analysis of crustal flow line transects crossing the Juan De Fuca Ridge (~0.15 km/s for layer velocities and 10–30 m for layer thickness for primarily off-axis data [*Nedimović et al.*, 2008]) which we attribute to better weather conditions during acquisition and consequently better data quality than obtained during the SEIR survey. In both studies, uncertainties in model solutions assume one-dimensional structure and actual uncertainties, in particular in regions of significant topographic variation, are expected to be higher.

[20] From velocity models obtained for each seismic line, the average velocity for layer $2A_{upper}$ and layer $2A_{lower}$ were computed. The two averages were then combined into a thickness weighted average for seismic layer 2A. For each cross-axis line, models within 1 km of the axis were averaged to determine on-axis velocity. Along some profiles, a near-axis increase in seismic velocities is observed with more gradual change further off axis. To compare changes in the near axis zone, we determined average velocity at a constant distance from the axis of 4.5 km corresponding to a crustal age of 125 ka. We also calculate percentage velocity

increase, defined as the percent difference between average on- and off-axis velocity relative to the on-axis velocity. For those profiles where off-axis velocities at 125 ka exceed on-axis values by more than 10%, we measure the width of the zone of velocity increase. This zone is defined as the region over which velocities increase by 90% of the difference between the average on-axis velocity and the off-axis velocity at 125 ka.

[21] The thicknesses of layer $2A_{upper}$ and layer $2A_{lower}$ are determined from model travel times and average velocities for these layers. Two-way travel times to the layer 2A event picked from the stacked sections were converted to depth using a 2D velocity model constructed for each line by linear interpolation between all CMP supergather velocity models for the line. Average thicknesses of layer 2A determined from models and stacked sections are given in Tables 1 and 2, which also include the percent off-axis thickening of 2A and width of zone of 2A thickening, estimated using the same criteria as for velocity.

4. Results

4.1. Layer 2A Velocity

[22] Along the ridge axis, layer 2A velocity ranges from an average of 3.0 ± 0.1 km/s at segment P1 to 2.8 ± 0.2 km/s at segment S1 (Table 1). The cross-axis data indicate a 10% increase in 2A velocity from zero age to 125 ka crust within segment P1 (0.3 km/s) and no significant change at segment P2 and S1 (Table 2). Further off axis, average layer 2A velocities determined from the axis-parallel transects at 550 ka crust (~20 km from the ridge axis), are higher at all 3 segments compared with zero age (Table 1 and Figure 9). However, a larger
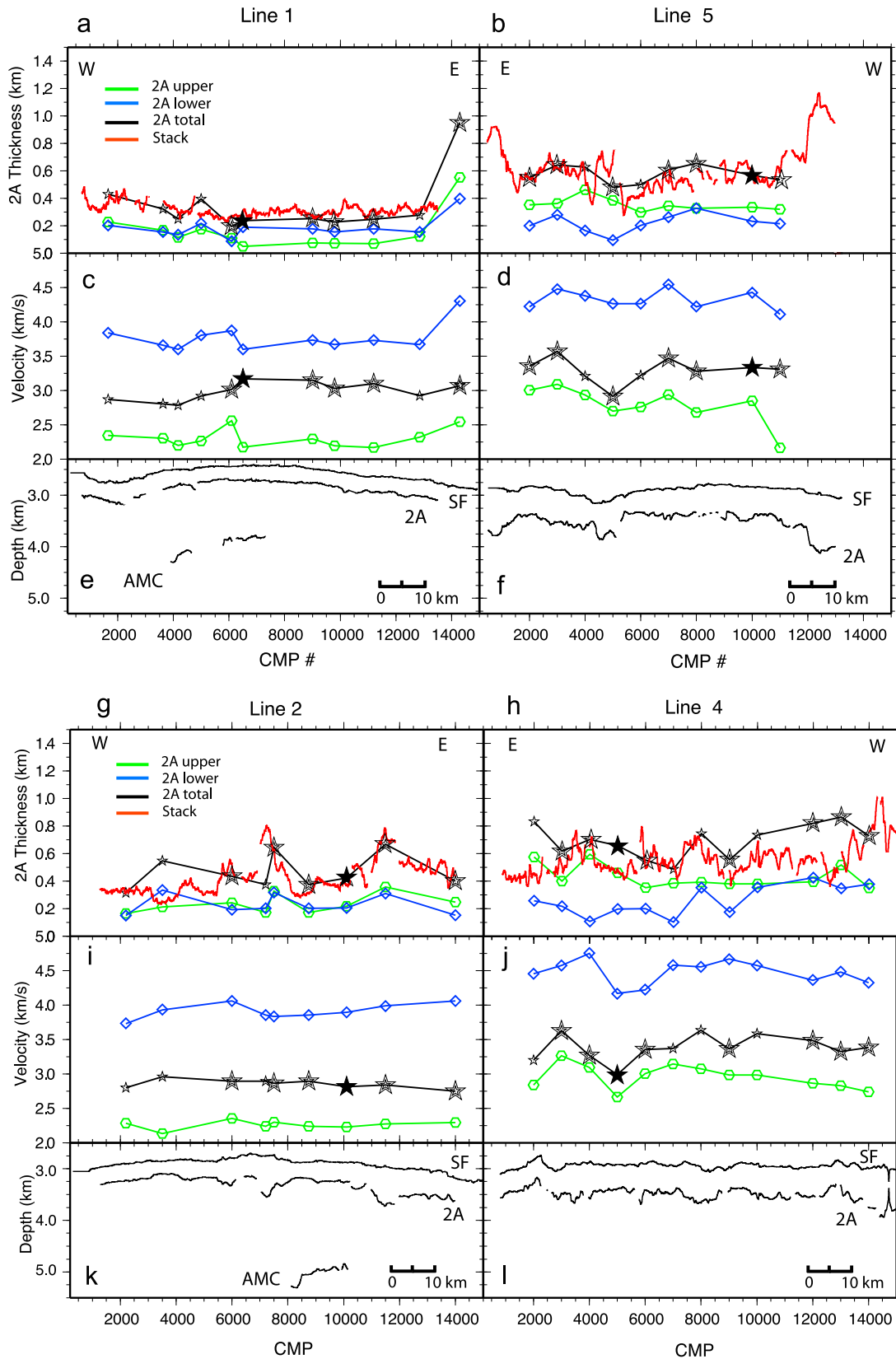
Figure 7
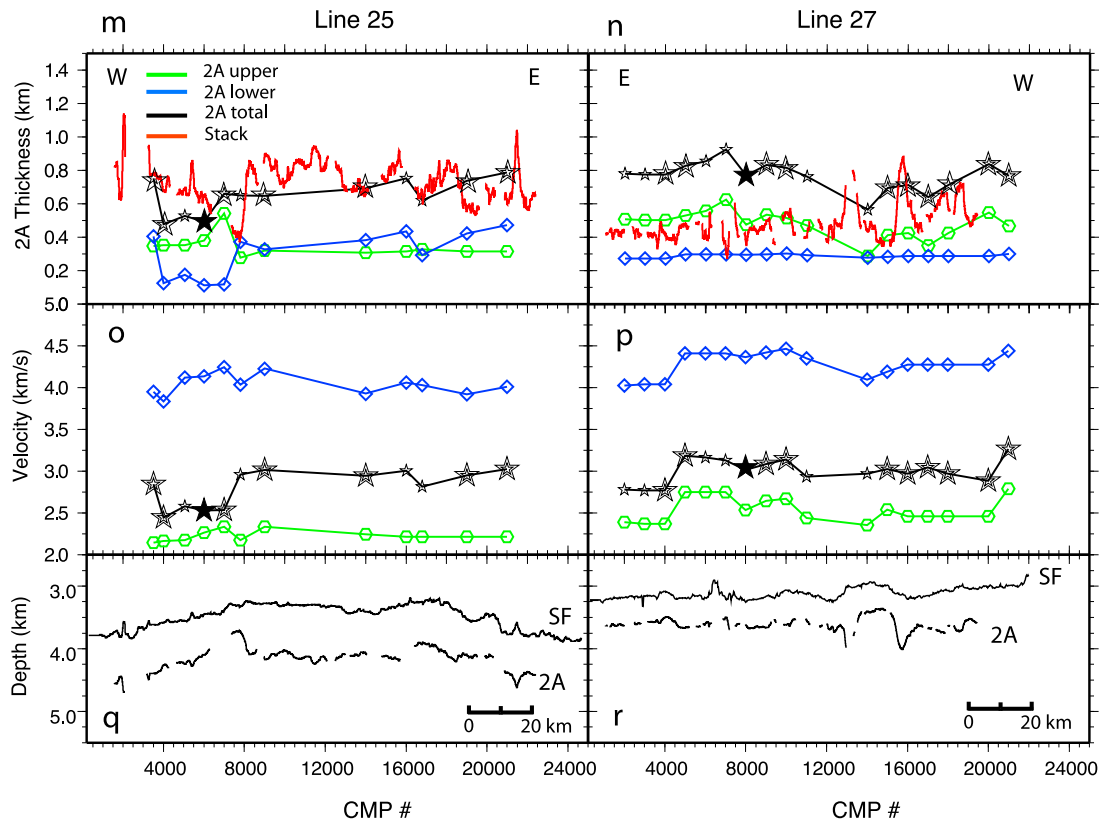
Figure 7. (continued)

overall increase in 2A velocity from zero age to 550 ka old crust is observed at segment P1 and P2 than at S1.

[23] From cross-axis lines, spatial variations in the presence of a near-axis (0–125 ka) zone of velocity increase are evident that appear correlated with where a magma lens is imaged in the crust. Along segment P1, velocities increase within the central portion of the segment including along both profiles where a magma lens is detected whereas no change in velocity is observed near the segment

end where the magma lens is absent (Figure 2a and Table 2). A resolvable increase in near-axis velocity is only observed along one line at segment P2, near the eastern end of the detected magma lens (Figure 2b). No near-axis velocity increase is observed at axial valley segment S1 (Figure 2c and Table 2).

4.2. Layer 2A Thickness

[24] Layer 2A doubles in thickness from zero age to 550 ka crust at segment P1, thickens by a lesser

Figure 7. Reflection section interpretation and traveltime modeling results for layer 2A velocity and thickness for each axis-parallel seismic profile from (a−f) segment P1, (g−l) segment P2, and (m−r) segment S1. Figures 7a, 7c, 7e, 7g, 7i, 7k, 7m, 7o, and 7q show results from along axis profiles, and Figures 7b, 7d, 7f, 7h, 7j, 7l, 7n, 7p, and 7r show results from off-axis profiles (550 ka crust). Figures 7e, 7f, 7k, 7l, 7q, and 7r show depth to seafloor, base of layer 2A, and magma lens (if imaged) from the migrated seismic sections (converted to depth using layer 2A velocities obtained from traveltime model results shown in Figures 7c, 7d, 7i, 7j, 7o, and 7p and a constant velocity of 5.5 km/s for layer 2B). Also shown are results for layer 2A velocity (Figures 7c, 7d, 7i, 7j, 7o, and 7p) and thickness (Figures 7a, 7b, 7g, 7h, 7m, and 7n) determined from each modeled CMP supergather. Average velocity and thickness for both sublayers of layer 2A as well as for whole layer are shown; green hexagons, layer $2A_{upper}$; blue diamonds, layer $2A_{lower}$; black stars, total layer 2A. Highest confidence velocity models determined from CMP supergathers with the clearest seismic arrivals are indicated with large stars. Solid black stars correspond with CMP gathers shown in Figures 4 and 5. In addition to 2A thickness estimated from modeled CMP supergathers, Figures 7a, 7b, 7g, 7h, 7m, and 7n also include the thickness of layer 2A (red line) determined from the stacked sections in Figures 7e, 7f, 7k, 7l, 7q, and 7r.
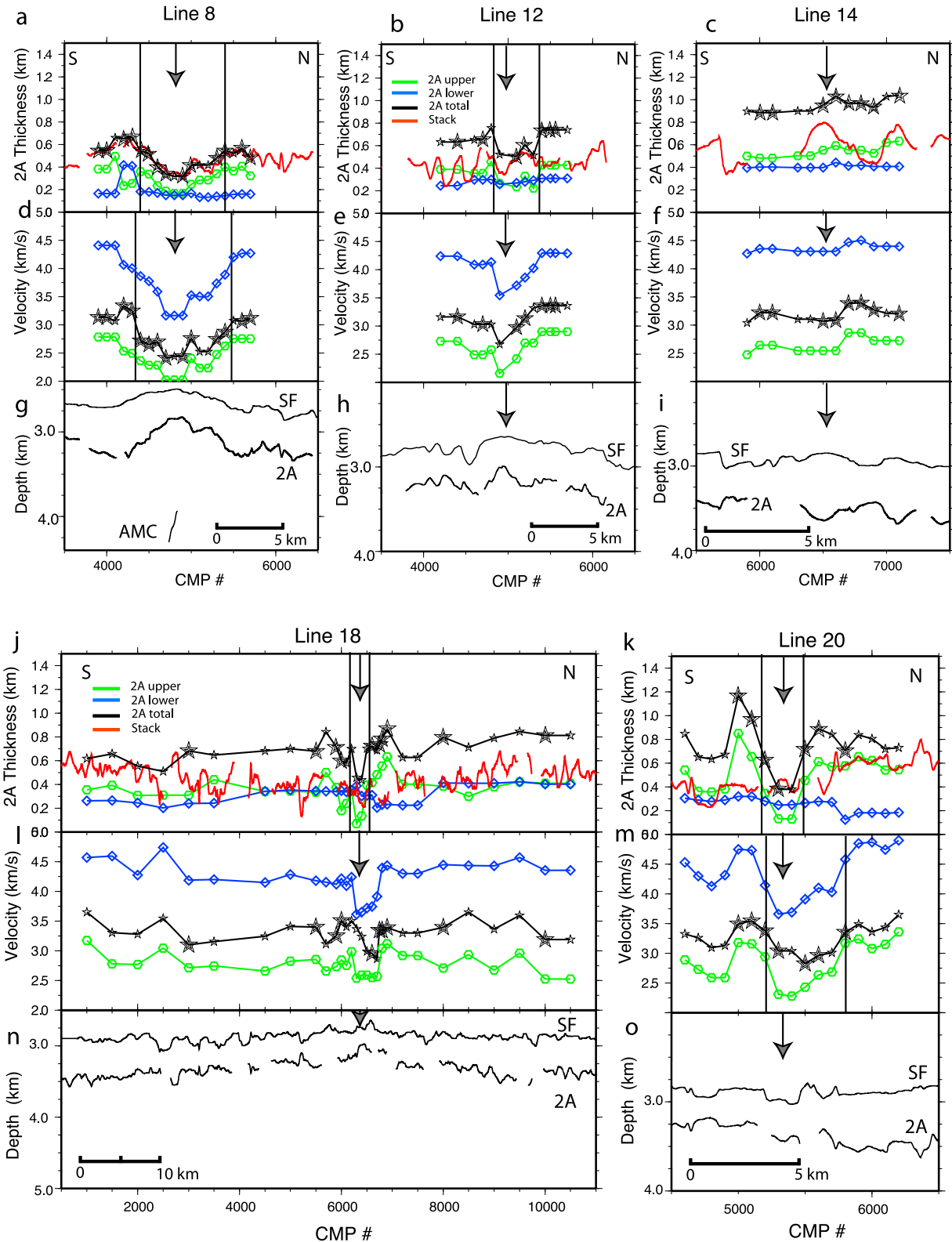
Figure 8. Reflection section interpretation and traveltime modeling results for layer 2A velocity and thickness for cross-axis seismic profiles from (a–i) segment P1, (j–o) segment P2, and (p–u) segment S1. Symbols and presentation of results are the same as in Figure 7. Black vertical lines delineate axial zone of 2A thickening and velocity increase where present (defined as zone over which 2A velocity and thickness reach 90% of off-axis values at 125 ka crust (see Table 2)). Black vertical arrows show location of ridge axis.
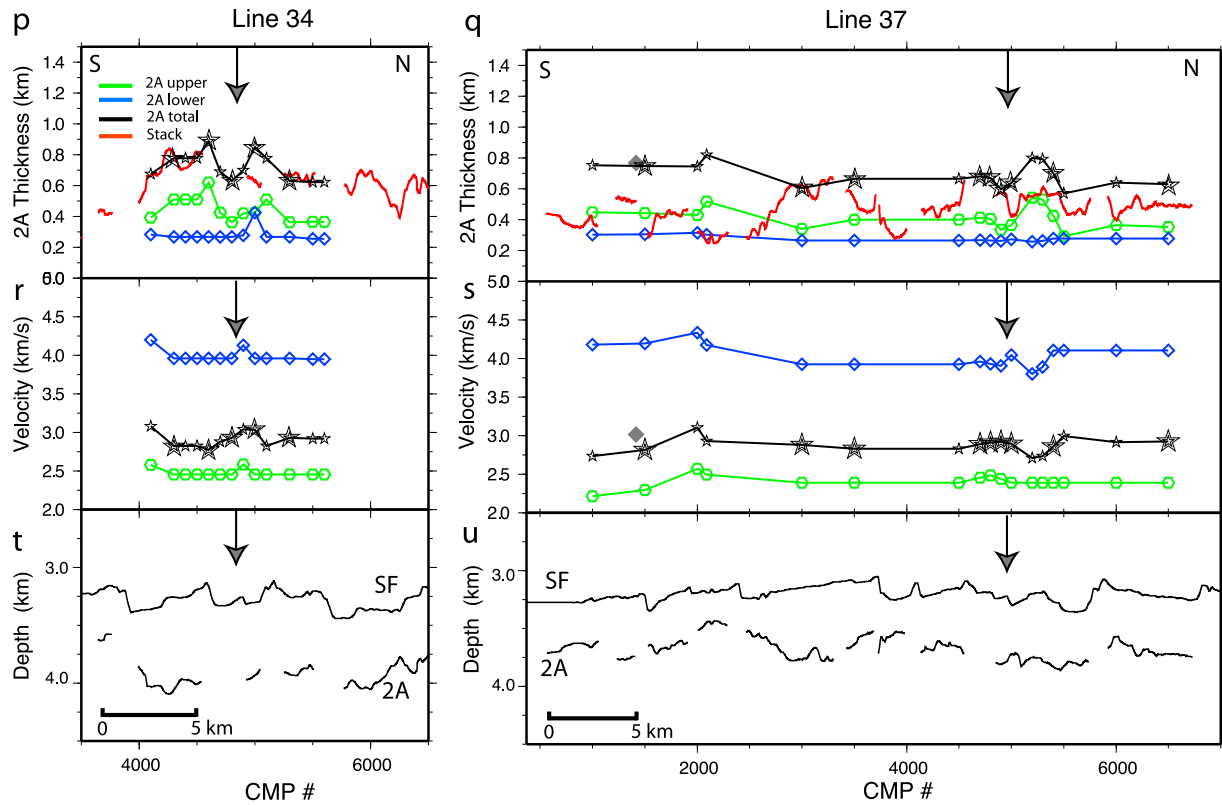
Figure 8. (continued)

amount (50%) at segment P2, with little off-axis thickening at S1 (Table 1 and Figure 9). Velocity modeling indicates that most of the increase in layer 2A thickness at segments P1 and P2 occurs in layer $2A_{upper}$ (Table 1). Although the largest 0–550 ka increase in layer 2A thickness is at segment P1, layer 2A is thinner at this segment than at segments P2, and S1 (P1: 570 ± 50 m, P2: 690 ± 100 m and

S1: 770 ± 80 m respectively). Most of these segment-to-segment differences arise from layer $2A_{upper}$; whereas the off-axis thickness of this layer is 350 ± 50 m at segment P1, it is 430 ± 90 m and 480 ± 80 m respectively at segments P2 and S1.

[25] Cross-axis data reveal increases in 2A thickness by 125 ka within segments P1 and P2 with

Table 1. Velocity and Thickness of Layer 2A From Axis-Parallel Lines

Velocity (km/s)	Segment P1			Segment P2			Segment S1		
	On Axis 0 ka[a]	Off Axis 550 ka[a]	% Increase[b]	On Axis 0 ka[a]	Off Axis 550 ka[a]	% Increase[b]	On Axis 0 ka[a]	Off Axis 550 ka[a]	% Increase[b]
2A upper	2.3 ± 0.1	2.8 ± 0.3	22%	2.3 ± 0.1	3.0 ± 0.2	30%	2.2 ± 0.1	2.7 ± 0.2	22%
2A lower	3.7 ± 0.1	4.3 ± 0.1	16%	4.0 ± 0.1	4.5 ± 0.2	12%	4.0 ± 0.1	4.5 ± 0.2	12%
Total 2A	3.0 ± 0.1	3.3 ± 0.2	10%	2.9 ± 0.1	3.4 ± 0.2	17%	2.8 ± 0.2	3.0 ± 0.1	NC
Top 2B	5.0 ± 0.1	5.7 ± 0.2	14%	5.4 ± 0.2	5.8 ± 0.2	7%	5.8 ± 0.2	5.9 ± 0.2	NC
Thickness (m)									
2A upper	120 ± 60	350 ± 50	200%	240 ± 70	430 ± 90	83%	350 ± 70	480 ± 80	33%
2A lower	170 ± 80	220 ± 60	33%	230 ± 130	260 ± 120	NC	300 ± 100	290 ± 90	NC
Total 2A	290 ± 70	570 ± 50	103%	470 ± 90	690 ± 100	49%	650 ± 320	770 ± 80	18%
Stacked data[c]	310 ± 40	620 ± 160	100%	420 ± 120	570 ± 110	34%	720 ± 110	490 ± 120	−31%

[a] Average values reported with one standard deviation.
[b] Percent difference between on-axis and off-axis averages. NC indicates no resolvable change given uncertainties of 0.2 km/s for velocity and 40 m for thickness (see section 3.2).
[c] Average thickness measured from stacked sections reported with one standard deviation.

Table 2. Velocity and Thickness of Layer 2A From Cross-Axis Lines

Segment and Line Number	Average Velocity on Axis[a] (km/s)	Average Velocity at 125 ka[b] (km/s)	% Velocity Increase at 125 ka[c]	Width of Velocity Increase Zone[d] (km)	Average 2A Thickness on Axis[a] (m)	Average 2A Thickness at 125 ka[b] (m)	% Thickening at 125 ka[c]	Stacked Data: Average 2A Thickness on Axis[a] (m)	Stacked Data: Average 2A Thickness at 125 ka[b] (m)	Stacked Data: % Thickening at 125 ka[c]	Width of Thickening Zone[d] (km)
P1											
8	2.5 ± 0.1	3.1 ± 0.2	24%	7.4	350 ± 40	570 ± 90	62%	370 ± 40	530 ± 80	43%	6.3
9	3.1 ± 0.3	3.4 ± 0.1	11%	2.7	490 ± 90	590 ± 160	20%	420 ± 30	530 ± 110	26%	7.4
10	2.8 ± 0.1	3.2 ± 0.1	14%	4.3	590 ± 50	600 ± 100	NC	340 ± 60	430 ± 170	26%	-
11	3.3 ± 0.2	3.5 ± 0.2	NC	-	700 ± 130	640 ± 60	−9%	420 ± 70	580 ± 140	38%	-
12	2.9 ± 0.2	3.2 ± 0.1	10%	-	520 ± 120	700 ± 50	35%	420 ± 50	450 ± 110	NC	3.4
13	3.0 ± 0.2	3.2 ± 0.1	NC	-	725 ± 10	790 ± 150	9%	400 ± 50	490 ± 110	23%	-
14	3.1 ± 0.1	3.2 ± 0.1	NC	-	950 ± 50	990 ± 60	NC	720 ± 90	730 ± 150	NC	-
Average[e]	3.0 ± 0.3	3.3 ± 0.1	10%		650 ± 200	700 ± 150	8%	420 ± 140	530 ± 100	26%	
P2											
15	3.0 ± 0.1	3.0 ± 0.1	NC	-	880 ± 40	980 ± 70	11%	560 ± 80	550 ± 100	NC	-
16	2.9 ± 0.1	3.0 ± 0.2	NC	-	670 ± 70	770 ± 120	15%	350 ± 50	460 ± 130	32%	3.6
17	3.2 ± 0.2	3.0 ± 0.1	NC	-	540 ± 80	820 ± 80	52%	450 ± 80	450 ± 90	NC	3.8
18	3.2 ± 0.2	3.3 ± 0.2	NC	-	530 ± 150	720 ± 100	36%	300 ± 60	460 ± 110	53%	1.8
19	3.0 ± 0.2	3.1 ± 0.1	NC	-	410 ± 50	630 ± 60	54%	330 ± 70	390 ± 90	19%	2.6
20	2.9 ± 0.1	3.4 ± 0.1	17%	3.8	410 ± 40	750 ± 60	83%	430 ± 80	530 ± 160	23%	2.0
Average[e]	3.0 ± 0.1	3.1 ± 0.2	NC		570 ± 170	780 ± 120	34%	400 ± 100	480 ± 60	20%	
S1											
34	3.0 ± 0.1	2.9 ± 0.1	NC	-	670 ± 40	680 ± 90	NC	650 ± 50	740 ± 100	14%	-
37	2.9 ± 0.1	2.9 ± 0.1	NC	-	620 ± 40	690 ± 40	11%	520 ± 60	470 ± 100	−10%	-
Average[e]	3.0 ± 0.1	2.9 ± 0.1	NC		645 ± 35	690 ± 50	NC	585 ± 100	610 ± 110	NC	

[a] On-axis velocity and thickness of Layer 2A defined as average within 1 km of ridge axis reported with one standard deviation.
[b] Average velocity and thickness of Layer 2A off axis at 125 ka reported with one standard deviation.
[c] Percent difference between on-axis and off-axis value at 125 ka relative to on-axis value. NC indicates no resolvable change given estimated uncertainties of 0.2 km/s for velocity and 40 m for thickness (see section 3.2).
[d] Defined as width of region over which velocity/thickness reaches 90% of off-axis value for those lines where off-axis velocity/thickness exceeds 10% of on-axis values.
[e] Average for all lines.
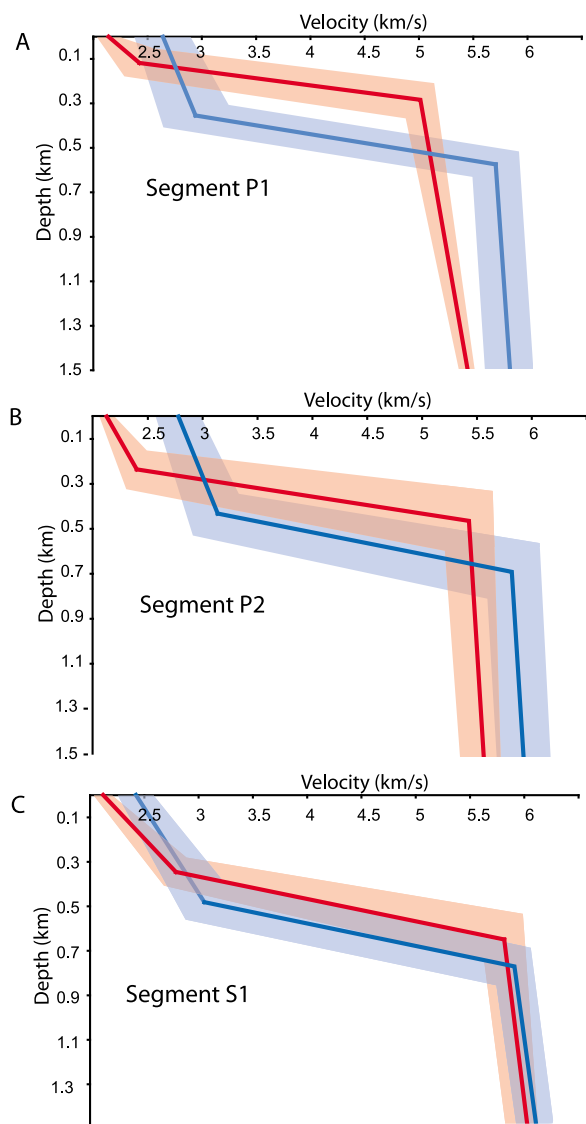
Figure 9. Velocity models for each investigated SEIR segment obtained from one-dimensional modeling of CMP supergathers from on-axis (red) and 550 ka (blue) isochron profiles. Bold line corresponds with average velocity model, and shaded area represents one standard deviation. Segment P1 shows significant change from on axis to off axis, whereas there is little change along segment S1.

spatial variations in the pattern of thickening within these segments. At segment P1, a wide zone of 2A thickening (up to 7.4 km) coincides with where the magma lens is imaged in the crust, whereas little cross axis thickening is observed on most lines away from where the magma lens is detected (Figure 2 and Table 2). At segment P2, resolvable thickening from 0 to 125 ka crust is evident along much of the segment but over a narrower zone (1.8–3.8 km) confined to within the shallow axial

valley present at this segment (Figure 2b and Table 2).

4.3. Layer 2B

[26] At zero-age crust, velocities determined for the top of layer 2B are lowest at segment P1 (5.0 ± 0.1 km/s), higher at segment P2 (5.4 ± 0.2 km/s) and highest at segment S1 (5.8 ± 0.2 km/s). Off-axis, layer 2B velocities increase by 14% at P1, 7% at P2, with no resolvable increase at S1 resulting in similar velocities of 5.7–5.9 km/s by 550 ka at all three segments (Table 1).

4.4. Comparison of 2A Structure Derived From Reflection Profiles and Models

[27] Along most axis-parallel lines, layer 2A thickness measured from the stacked data coincides well with total layer 2A thickness obtained from modeling of CMP supergathers (Table 1). However, significant mismatch is observed along the 550 ka isochron line (line 27) at segment S1 and along most cross-axis lines. Along line 27, layer 2A thicknesses obtained from the stacked sections are thinner than the total thickness of layer 2A determined from the models but coincide well with the thickness of $2A_{upper}$ (Table 1 and Figures 7m–7r). For most cross-axis lines, layer 2A thickness measured from the reflection profiles coincide with model estimates only within the axial region. Off-axis, reflection profile derived estimates are comparable to or slightly greater than the thickness of layer $2A_{upper}$ obtained from the CMP gather models (Figure 8).

5. Discussion

5.1. Layer 2A Velocity

[28] Layer 2A velocities increase from zero age to 550 ka old crust at all three segments of the SEIR studied with larger increases at segments P1 and P2 than axial valley segment S1. The observed changes are consistent with global compilations of layer 2A velocities with crustal age (Figure 10) [Carlson, 1998; Grevemeyer et al., 1999] and are believed to primarily reflect gradual infill of pore spaces in the upper crust with secondary alteration minerals due to hydrothermal fluid circulation [e.g., Jacobson, 1992]. A two-stage evolution of layer 2A velocities (rapid at young ages with a more gradual increase to ~10 my) is apparent in the existing global compilations, which Grevemeyer and Weigel [1997] attribute to different rates of
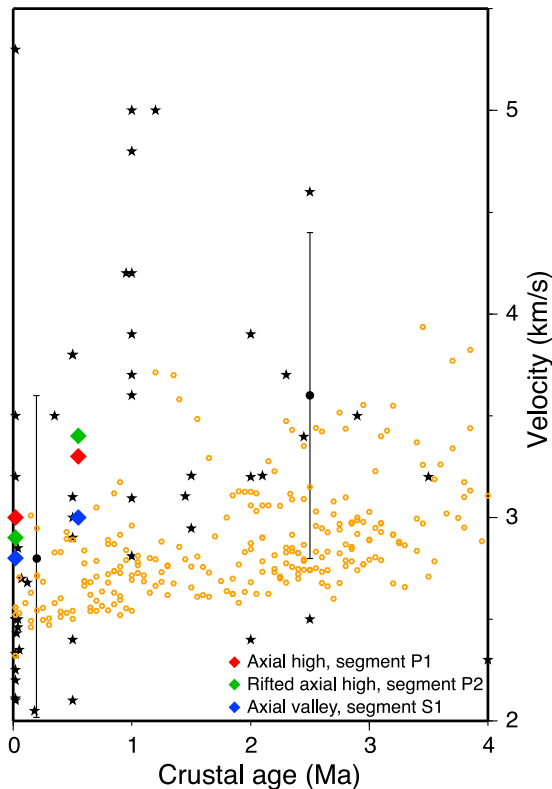
Figure 10. Average layer 2A P wave velocities for the isochron lines along the three segments investigated in this study (solid colored diamonds) are shown together with average layer 2A velocity results from other studies around the globe as a function of crustal age and for the first 4 Ma of crustal evolution. Black stars are both velocities compiled by *Carlson* [1998] for years 1976 to 1997 and velocities from *Grevemeyer et al.* [1999] from an investigation designed to study upper crustal aging along the East Pacific Rise at 14°S. Solid black circles with error bars are mean velocities from *Carlson* [1998] for ages <1 and 1–5 Ma. Orange hexagons are average layer 2A velocities from the Juan de Fuca ridge and its flanks [*Nedimović et al.*, 2008]. Juan de Fuca ridge is also spreading at intermediate rates. Modified from *Nedimović et al.* [2008].

crustal alteration associated with ridge axis and flank hydrothermal activity. Along the SEIR, we find differences in the rate of change in seismic properties at youngest crustal ages for the three segments studied that are likely linked to the vigor of ridge axis hydrothermal activity associated with the presence/absence of crustal magma bodies. A larger increase in velocity off axis is measured at segments P1 and P2, where magma bodies are detected for part of each segment (Table 1). At segment P1, velocities increase by 10% from 0 to 125 ka crust with no further change at 550 ka crust indicating rapid alteration within the near axis region. At segment S1 where a magma lens is

absent beneath the innermost axial region, no near-axis increase in 2A velocity is detected.

[29] In addition to these differences in seismic properties between segments, there is evidence for spatial variations within a segment linked to proximity of crustal magma bodies. Within segment P1, a larger increase in 2A velocity is observed and over a wider zone along cross-axis lines where a magma lens is detected in the subsurface (Table 2 and Figure 2). These observations link a rapid, near-axis increase in velocity of the uppermost crust to regions where elevated axial thermal structure and greater ridge axis hydrothermal activity is expected. Changes in physical properties of the upper crust due to secondary mineralization will depend strongly on the temperature of reaction and water/rock ratios linked to crustal porosity and permeability. Where magma bodies are present, higher temperatures in the upper crust, more vigorous hydrothermal flow, and higher rates and extents of alteration are expected.

[30] In some studies of upper crustal velocity structure, azimuthal anisotropy in compressional wave velocities has been detected with fast direction parallel to the ridge axis. *Mcdonald et al.* [1994] report significant anisotropy within upper 500 m of the crust at Cleft segment of the Juan de Fuca Ridge, which they attributed to presence of open fractures aligned in the ridge axis direction. Further north at the Endeavor segment of the Juan de Fuca Ridge, *Cudrak and Clowes* [1993] find evidence for azimuthal anisotropy within layer 2 at the ridge axis but not in older crust. Along the SEIR, layer 2A velocities obtained from modeling of across and along-axis data are comparable, and there is no indication of upper crustal anisotropy in the shallowest crust. However, it is important to note that the 1-D modeling approach used in our study is not well suited for assessing anisotropy because P wave velocities are best constrained only in the along axis direction where topographic variations are minimal.

5.2. Thickening of Seismic Layer 2A

[31] Our study reveals significant differences in the magnitude and pattern of layer 2A thickening away from the ridge axis at each of the three segments. The greatest change in layer 2A thickness from 0 to 550 ka is found at axial high segment P1 (100%), with 50% thickening at the rifted axial high segment P2, and only 18% thickening at axial valley segment S1. Differences in total layer 2A thickness are also observed with the thinnest layer 2A, both

on and off axis, at P1 and thickest 2A at S1 (Table 1). At segment P1, the widest thickening zone and greatest percent thickening are found along cross-axis lines near where a magma lens is detected in the subsurface beneath the shallow, broad portions of this segment (Figure 2a). Along most of segment P2, a ~2–4 km wide zone of 2A thickening is observed which is confined to the axial rift defined by the first inward facing faults bounding the ridge axis (Figure 2b).

[32] Studies from other intermediate spreading ridges show similar variations in layer 2A characteristics with axial morphology including thinner 2A at zero age and greater thickening away from the axis at shallow broad axial high segments compared with deeper rifted segments. At the Galapagos Spreading Center (GSC), the magnitude of off-axis thickening is greatest where an axial high is present close to the Galapagos hot spot, decreasing to the west as the axis evolves to a rifted and transitional axial morphology [*Blacic et al.*, 2004]. At the Juan de Fuca Ridge, layer 2A thickens by 60–90% at the shallow broad Vance and Cleft segments, whereas no clear pattern of thickening is evident at the deeper, narrower Endeavor segment to the north [*Canales et al.*, 2005; *Van Ark et al.*, 2007]. At zero age, a thin more uniform layer 2A is found along the axis of Cleft and Vance segments compared with Endeavor segment [*Carbotte et al.*, 2006], similar to the contrast in 2A characteristics at axial high segment P1 and axial valley segment S1 (Table 1).

[33] In most previous studies, the pattern of off-axis thickening of 2A has been interpreted in terms of volcanic emplacement processes including off-axis volcanism, the length of lava flows linked to lava effusion rates, local bathymetric slopes, and to the presence of possible obstruction to flow such as nearby faults, [e.g., *Hooft et al.*, 1996; *Carbotte et al.*, 2000; *Blacic et al.*, 2004]. Segment-to-segment variations observed along the SEIR are also consistent with thickening of layer 2A via volcanic processes. Downslope transport of lavas promoted by bathymetric gradients associated with the axial high topography of segment P1 could account for the greater percent thickening observed at this segment. The correlation between width of the 2A thickening zone and the width of the shallow axial valley or graben at segment P2 is consistent with damming of lava flows by the valley walls. Layer 2A observations from the GSC also suggest that the axial graben found along part of this spreading center may act as a barrier to 2A thick-

ening [*Canales et al.*, 2005; *Blacic et al.*, 2004]. However, observations from the Cleft segment of the JdFR, where over 50% of 2A thickening is observed beyond the axial graben walls, are inconsistent with this mechanism [*Canales et al.*, 2005].

[34] An alternate hypothesis is that off-axis thickening of layer 2A may be linked to downward propagation of a cracking or alteration front [e.g., *McClain et al.*, 1985; *Christeson et al.*, 2007]. In this scenario, greater off-axis thickening at axial high segment P1 and rifted high segment P2 would imply enhanced downward cracking compared with axial valley segment S1. With crustal magma bodies present at segments P1 and P2, larger thermal gradients within the upper crust are expected which could be associated with enhanced cracking and migration of alteration fronts associated with hydrothermal flow. We favor volcanic processes linked to axial morphology, in particular downslope transport of lavas promoted by axial high relief of segment P1 and damming of lavas within the shallow rift at segment P2, to account for the patterns of 2A thickening observed at the SEIR. However, based on the available observations, the cracking/alteration hypothesis cannot be ruled out. The migration of cracking or alteration fronts associated with hydrothermal processes and off-axis accumulation of lavas are both plausibly linked to the thermal structure of the axis and distribution of crustal magma bodies. Both processes may contribute to the off-axis thickening of 2A.

5.3. Evolution of Layer 2B

[35] Observations for uppermost layer 2B indicate that seismic velocities within this part of the crust also evolve from 0 to 550 ka, and that changes are linked to ridge segment structure. At zero age, layer 2B velocities are significantly lower at segments P1 and P2 (5.0 ± 0.1km/s and 5.4 ± 0.2 km/s) than at segment S1 (5.8 ± 0.2 km/s). Within 550 ka crust, similar high 2B velocities of 5.7–5.9 km/s are measured at all three segments, which corresponds with a 14% and 7% increase at P1 and P2 respectively, but little change at S1. Differences in layer 2A thickness accompany these variations in 2B velocity with thinner 2A where 2B velocities are lower (Table 1). Lower overburden pressures and more open cracks where layer 2A is thin likely contribute to the slower on-axis velocities in shallowest 2B at segments P1 and P2. Velocity gradients in layer 2B estimated from the coincident OBS seismic refraction study of *Holmes et al.* [2008] for segments P1, P2 and S1 are well con-

strained for depths > 1km below seafloor where gradients of 0.6 to 0.75 s^{-1} are measured. From these gradients, we estimate up to 30% of the observed off-axis increase in 2B velocity at P1 and 40% of the increase at P2 could reflect the impact of the thicker 2A in older crust, and decreased porosities in shallow 2B due to increasing overburden.

[36] However, to fully account for the segment-scale differences in 2B velocities and off-axis evolution, other factors must be important. Direct observations of tectonic exposures at Hess Deep reveal intense brittle deformation within the dike and lava section [*Karson et al.*, 2002a], which is attributed to axial subsidence and caldera collapse with inflation/deflation of an underlying steady state crustal magma body. With crustal magma bodies present at both segments P1 and P2, similar subaxial deformation linked to magmatic processes may well contribute to low axial 2B velocities at these segments. Enhanced microcracking within the dike section associated with vigorous on-axis hydrothermal activity driven by the underlying crustal heat sources [e.g., *Tolstoy et al.*, 2008] could also contribute. Crack closure on the ridge flanks due to thickening overburden and crack infill with alteration products could act to increase 2B velocities at these segments to values comparable to segment S1 where extensive magmatic subsidence and on-axis hydrothermal cracking are suppressed. Cooling of the dike section as it moves out of the ridge axis volcanic and hydrothermal regime may also contribute to increasing 2B velocities in older crust (0.2 km/s increase in velocity expected for a temperature decrease of 500° to 0° [*Christensen*, 1979]).

[37] As a final comment, it is important to note that 2B velocities obtained in this study are averages for some depth interval of uppermost 2B that is not well constrained and will vary depending on the seafloor topography, water depth, presence or absence of sediments, and seismic structure of the overlying 2A layer. Comparisons of shallowest 2B velocities from 1D forward modeling must be made with caution and are better constrained with a 2D tomographic approach and good constraints on velocity structure of the overlying 2A layer [e.g., *Newman et al.*, 2007].

5.4. Comparison of Layer 2A Thickness Estimated From Reflection Sections and Modeling

[38] Along many of the profiles studied, the thickness of layer 2A measured from the reflection sections is lower than thicknesses obtained from modeling of coincident CMP supergathers (Figures 7n and 8). Similar mismatch has been observed in other studies [e.g., *Van Ark et al.*, 2007; *Hussenoeder et al.*, 2002a], with the layer 2A pseudoreflection at some sites located at shallower depths than the base of layer 2A identified from velocity modeling. In our study, the largest discrepancies are observed for lines shot perpendicular to the ridge axis where, in general, good agreement between the layer 2A event in the stacked sections and the base of layer 2A in coincident velocity models is only observed right at the ridge axis (Figure 8 and Table 2). Mismatch seen at line crossings between axis-parallel and axis-perpendicular profiles (Figures 7 and 8 and Tables 1 and 2), are likely due to faulting or imaging issues associated with steep bathymetry and the wide-angle nature of the layer 2A event [e.g., *Harding et al.*, 1993]. However, the systematic mismatch between velocity models and reflection sections along axis-perpendicular lines likely arises from structure within layer 2A$_{lower}$ that is unresolved in our velocity models. From their modeling study of layer 2A velocity structure, *Christeson et al.* [1996] conclude that the correlation of the layer 2A event in reflection sections with the base of layer 2A is strongly dependent on structure within this layer. *Christeson et al.* [1996] model synthetic shot gathers and stacked sections for two different shallow crustal velocity structures derived from observations at the EPR 9°30′N; one with a single high velocity gradient defining layer 2A$_{lower}$ and one with a two step high-gradient zone. They find that for the complex gradient case, the 2A event coincides with the shallowest high-gradient within layer 2A$_{lower}$, whereas for a simple linear velocity gradient, the 2A horizon stacks at travel times that coincide well with the bottom of layer 2A.

[39] Along most of our cross-axis lines, the thickness of layer 2A estimated from the stacked data roughly coincides with the thickness of layer 2A$_{upper}$ implying that the stacked horizon falls near the top of the high gradient zone within layer 2A rather than the base of it. Along axis-parallel lines, mismatch between the models and reflection sections is only observed along the 550 ka isochron profile of segment S1 indicating a complex, possibly step gradient zone may be present at this off-axis location. These observations reinforce the conclusions of *Christeson et al.* [1996] that independent constraints on 2A velocity structure are needed to properly interpret

patterns of layer 2A thickness obtained from CMP reflection sections.

6. Summary

[40] The main findings of our study of the evolution of the upper crust from three contrasting segments of the SEIR are summarized below:

[41] 1. P wave velocities within layer 2A increase in the first 550 ka of crustal formation at all SEIR segments, consistent with observations elsewhere and are attributed to infill of crustal porosity with hydrothermal precipitates during fluid circulation within the uppermost crust. Velocity changes in layer 2A are larger at axial high segment P1 and rifted axial high segment P2 than at axial valley segment S1 indicating higher rates of alteration, which we attribute to elevated axial thermal structure at these segments.

[42] 2. At younger crustal ages (125 ka), P wave velocities increase more rapidly at segment P1 than at segments P2 and S1. Along-axis variations are also observed within segment P1 with larger increase in layer 2A velocity and over a wider region near where a magma lens is present in the crust. These observations indicate that upper crustal evolution is linked to proximity of crustal magma bodies presumably through more vigorous ridge axis hydrothermal activity and elevated temperatures of reaction resulting in increased mineral precipitation and infill of crustal porosity.

[43] 3. Layer 2A thickens away from the axis with variations in the rate and magnitude of thickening with axial structure. The largest percent off-axis thickening is observed at axial high segment P1, and least at axial valley segment S1. Spatial variations are observed within segment P1 in the width of the zone of thickening with the widest zone near where a magma body is present and the axial high is broad and shallow. The greater thickening at the axial high segment is most readily explained by accumulation of lavas through off-axis transport of flows promoted by the downslope topography of the axial high. Volcanic controls on layer 2A thickening are also supported by observations from segment P2, where the zone of off-axis thickening is confined within the walls of the shallow axial rift present at this segment. Downward propagation of a cracking or alteration front linked to ridge axis hydrothermal activity could also contribute to the patterns of off-axis 2A thickening. The two mechanisms are not mutually exclusive and both are plausibly linked to axial magmatic and thermal structure.

[44] 4. In zero-age crust, velocities within shallowest layer 2B are lower at segments P1 and P2 compared with S1 whereas similar velocities are measured at all three segments in crust 550 ka old. Low on-axis 2B velocities at segments P1 and P2 can be attributed, in part, to thinner layer 2A at these segments with higher porosities expected in shallowest 2B due to lower overburden pressures. However, differences in layer 2A thickness cannot fully account for the segment-to-segment differences in 2B and other factors must be important. Magmatic and hydrothermal processes linked to crustal magma bodies which are present at both segments P1 and P2 but not S1 may play a key role. Enhanced subaxial deformation due to magmatic subsidence and dike intrusion along with extensive cracking of the dike section during on-axis hydrothermal activity driven by crustal heat sources may decrease porosities in the axial upper crust contributing to low 2B velocities. The off-axis increase in 2B velocities at these segments is attributed to crack closure with thickening overburden and crack infill with alteration products during hydrothermal flow.

[45] 5. In some locations, the thickness of layer 2A estimated from reflection sections corresponds more closely with the thickness of the low gradient upper portion of layer 2A (layer $2A_{lupper}$) than with the total 2A thickness derived from velocity modeling of CMP supergathers. This mismatch is likely due to variations in the structure of layer $2A_{lower}$ with the reflection sections imaging the top of this zone of high velocity gradient in regions of complex structure [e.g., *Christeson et al.*, 1996].

Acknowledgments

References

Alt, J. C., J. Honnorez, C. Laverne, and R. Emmermann (1986), Hydrothermal alteration of a 1 km section through

the upper oceanic crust, Deep Sea Drilling Project Hole 504B: Mineralogy, chemistry, and evolution of seawater-basalt interactions, *J. Geophys. Res.*, *91*, 10,309–10,335, doi:10.1029/JB091iB10p10309.

Baran, J. M., J. R. Cochran, S. M. Carbotte, and M. R. Nedimović (2005), Variations in upper crustal structure due to variable mantle temperature along the Southeast Indian Ridge, *Geochem. Geophys. Geosyst.*, *6*, Q11002, doi:10.1029/2005GC000943.

Becker, K., et al. (1989), Drilling deep into young oceanic crust, Hole-504b, Costa Rica Rift, *Rev. Geophys.*, *27*, 79–102, doi:10.1029/RG027i001p00079.

Blacic, T. M., G. Ito, J. P. Canales, R. S. Detrick, and J. Sinton (2004), Constructing the crust along the Galapagos Spreading Center 91.3°–95.5°W: Correlation of seismic layer 2A with axial magma lens and topographic characteristics, *J. Geophys. Res.*, *109*, B10310, doi:10.1029/2004JB003066.

Canales, J. P., R. S. Detrick, S. M. Carbotte, G. M. Kent, J. B. Diebold, A. Harding, J. Babcock, M. R. Nedimović, and E. van Ark (2005), Upper crustal structure and axial topography at intermediate spreading ridges: Seismic constraints from the southern Juan de Fuca Ridge, *J. Geophys. Res.*, *110*, B12104, doi:10.1029/2005JB003630.

Carbotte, S. M., J. C. Mutter, and L. Xu (1997), Contribution of tectonism and volcanism to axial and flank morphology of the southern EPR from a study of Layer 2A, *J. Geophys. Res.*, *101*, 10,165–10,184.

Carbotte, S. M., G. Ponce-Correa, and A. Solomon (2000), Evaluation of morphological indicators of magma supply and segmentation from a seismic reflection study of the EPR 15°30′–17°N, *J. Geophys. Res.*, *105*, 2737–2759.

Carbotte, S. M., R. S. Detrick, A. Harding, J. P. Canales, J. Babcock, G. Kent, E. Van Ark, M. Nedimovic, and J. Diebold (2006), Rift topography linked to magmatism at the intermediate spreading Juan de Fuca Ridge, *Geology*, *34*, 209–212, doi:10.1130/G21969.1.

Carlson, R. L. (1998), Seismic velocities in the uppermost oceanic crust: Age dependence and the fate of layer 2A, *J. Geophys. Res.*, *103*, 7069–7077, doi:10.1029/97JB03577.

Christensen, N. I. (1979), Compressional wave velocities in rocks at high-temperatures and pressures, critical thermal gradients, and crustal low-velocity zones, *J. Geophys. Res.*, *84*, 6849–6857, doi:10.1029/JB084iB12p06849.

Christeson, G. L., G. M. Kent, G. M. Purdy, and R. S. Detrick (1996), Extrusive thickness variability at the East Pacific Rise, 9°–10°N: Constraints from seismic techniques, *J. Geophys. Res.*, *101*, 2859–2873, doi:10.1029/95JB03212.

Christeson, G. L., K. D. McIntosh, and J. A. Karson (2007), Inconsistent correlation of seismic layer 2a and lava layer thickness in oceanic crust, *Nature*, *445*, 418–421, doi:10.1038/nature05517.

Cochran, J. R., J. C. Sempere, and SEIR Scientific Team (1997), The Southeast Indian Ridge between 88°E and 120°E: Gravity anomalies and crustal accretion at intermediate spreading rates, *J. Geophys. Res.*, *102*, 15,463–15,487.

Cudrak, C. F., and R. M. Clowes (1993), Crustal structure of Endeavour Ridge Segment, Juan de Fuca Ridge, from a detailed seismic refraction survey, *J. Geophys. Res.*, *98*, 6329–6349.

DeMets, C., R. G. Gordon, D. F. Argus, and S. Stein (1994), Effect of recent revisions to the geomagnetic reversal time scale on estimates of current plate motions, *Geophys. Res. Lett.*, *21*, 2191–2194, doi:10.1029/94GL02118.

Forsyth, D. W., R. L. Ehrenbard, and S. Chapin (1987), Anomalous upper mantle beneath the Australian-Antarctic Discor-dance, *Earth Planet. Sci. Lett.*, *84*, 471–478, doi:10.1016/0012-821X(87)90011-2.

Francheteau, J., R. Armijo, J. L. Cheminee, R. Hekinian, P. Lonsdale, and N. Blum (1990), 1 Ma East Pacific Rise oceanic crust and uppermost mantle exposed by rifting in Hess Deep (equatorial Pacific Ocean), *Earth Planet. Sci. Lett.*, *101*, 281–295, doi:10.1016/0012-821X(90)90160-Y.

Grevemeyer, I., and A. Bartetzko (2004), Hydrothermal aging of oceanic crust; inferences from seismic refraction and bore-hole studies, in *Hydrogeology of the Oceanic Lithosphere*, edited by E. E. Davis and H. Elderfield, pp. 128–150, Cambridge Univ. Press, Cambridge, U. K.

Grevemeyer, I., and W. Weigel (1997), Increase of seismic velocities in upper oceanic crust: The "superfast" spreading East Pacific Rise at 14°14′S, *Geophys. Res. Lett.*, *24*, 217–220, doi:10.1029/96GL04005.

Grevemeyer, I., N. Kaul, H. Villinger, and W. Weigel (1999), Hydrothermal activity and the evolution of the seismic properties of upper oceanic crust, *J. Geophys. Res.*, *104*, 5069–5079, doi:10.1029/1998JB900096.

Harding, A. J., G. M. Kent, and J. A. Orcutt (1993), A multichannel seismic investigation of the upper crustal structure at 9°N on the East Pacific Rise: Implications for crustal accretion, *J. Geophys. Res.*, *98*, 13,925–13,944.

Holmes, R. C., M. Tolstoy, J. R. Cochran, and J. S. Floyd (2008), Crustal thickness variations along the Southeast Indian Ridge (100°–116°E) from 2-D body wave tomography, *Geochem. Geophys. Geosyst.*, *9*, Q12020, doi:10.1029/2008GC002152.

Hooft, E. E. E., H. Schouten, and R. S. Detrick (1996), Constraining crustal emplacement processes from the variation of seismic layer 2A thickness at the East Pacific Rise, *Earth Planet. Sci. Lett.*, *142*, 289–310, doi:10.1016/0012-821X(96)00101-X.

Houtz, R., and J. I. Ewing (1976), Upper crustal structure as a function of age, *J. Geophys. Res.*, *81*, 2490–2498, doi:10.1029/JB081i014p02490.

Hussenoeder, S. A., R. S. Detrick, G. M. Kent, H. Schouten, and A. J. Harding (2002a), Fine-scale seismic structure of young upper crust at 17°20′S on the fast spreading East Pacific Rise, *J. Geophys. Res.*, *107*(B8), 2158, doi:10.1029/2001JB001688.

Hussenoeder, S. A., G. M. Kent, and R. S. Detrick (2002b), Upper crustal seismic structure of the slow spreading Mid-Atlantic Ridge, 35°N: Constraints on volcanic emplacement processes, *J. Geophys. Res.*, *107*(B8), 2156, doi:10.1029/2001JB001691.

Jacobs, A. M., A. J. Harding, and G. M. Kent (2007), Axial crustal structure of the Lau back-arc basin from velocity modeling of multichannel seismic data, *Earth Planet. Sci. Lett.*, *259*, 239–255, doi:10.1016/j.epsl.2007.04.021.

Jacobson, R. S. (1992), Impact of crustal evolution on changes of the seismic properties of the uppermost ocean crust, *Rev. Geophys.*, *30*, 23–42, doi:10.1029/91RG02811.

Johnson, H. P., and J. E. Pariso (1987), The effect of hydrothermal alteration on the magnetic properties of oceanic crust: Results from drillholes CY-2 and CY-2a, Cyprus Study project, in *Cyprus Crustal Studies Project: Initial Reports, Holes CY-2 and 2a*, edited by P. T. Robertson, I. L. Gibson, and A. Panayiotou, pp. 283–293, Geol. Surv. of Can., Ottawa, Ont., Canada.

Juteau, T., D. Bideau, O. Dauteuil, G. Manach, D. D. Naidoo, P. Nehlig, H. Ondreas, M. A. Tivey, K. X. Whipple, and J. R. Delaney (1995), A submersible study in the western Blanco fracture zone, NE Pacific—Structure and evolution during

the last 1.6 Ma, *Mar. Geophys. Res.*, *17*, 399–430, doi:10.1007/BF01371786.

Karson, J. A., et al. (2002a), Structure of uppermost fast-spread oceanic crust exposed at the Hess Deep Rift: Implications for subaxial processes at the East Pacific Rise, *Geochem. Geophys. Geosyst.*, *3*(1), 1002, doi:10.1029/2001GC000155.

Karson, J. A., M. A. Tivey, and J. R. Delaney (2002b), Internal structure of uppermost oceanic crust along the Western Blanco Transform Scarp: Implications for subaxial accretion and deformation at the Juan de Fuca Ridge, *J. Geophys. Res.*, *107*(B9), 2181, doi:10.1029/2000JB000051.

Kent, G. M., A. J. Harding, J. A. Orcutt, R. S. Detrick, J. C. Mutter, and P. Buhl (1994), Uniform accretion of oceanic crust south of the Garrett transform at 14°15′S on the East Pacific Rise, *J. Geophys. Res.*, *99*, 9097–9116, doi:10.1029/93JB02872.

Klein, E. M., C. H. Langmuir, A. Zindler, H. Staudigal, and B. Hamelin (1988), Isotopic evidence of a mantle convecting boundary at the Australian-Antarctic discordance, *Nature*, *333*, 623–629, doi:10.1038/333623a0.

Kuster, G. T., and M. N. Toksoz (1974), Velocity and attenuation of seismic waves in 2-phase media. 1. Theoretical formulations, *Geophysics*, *39*, 587–606, doi:10.1190/1.1440450.

Ma, Y., and J. R. Cochran (1996), Transitions in axial morphology along the Southeast Indian Ridge, *J. Geophys. Res.*, *101*, 15,849–15,866.

McClain, J. S., J. A. Orcutt, and M. Burnett (1985), The East Pacific Rise in cross section: A seismic model, *J. Geophys. Res.*, *90*, 8627–8639, doi:10.1029/JB090iB10p08627.

McDonald, M. A., J. A. Hildebrand, and S. C. Webb (1994), Seismic structure and anisotropy of the Juan de Fuca Ridge at 45°N, *J. Geophys. Res.*, *99*, 4857–4874.

Nedimović, M. R., S. M. Carbotte, J. B. Diebold, A. J. Harding, J. P. Canales, and G. M. Kent (2008), Upper crustal evolution across the Juan de Fuca ridge flanks, *Geochem. Geophys. Geosyst.*, *9*, Q09006, doi:10.1029/2008GC002085.

Newman, K. R., M. R. Nedimovic, J. P. Canales, and S. M. Carbotte (2007), Upper crustal evolution along the Juan de Fuca Ridge flanks from travel time tomography of seismic layer 2, *Eos Trans. AGU*, *88*(52), Fall Meet. Suppl., Abstract S12A-07.

Nicolas, A. (1989), *Structure of Ophiolites and Dynamics of Oceanic Lithosphere*, 376 pp., Kluwer Acad., Dordrecht, Netherlands.

Purdy, G. M. (1987), New observations of the shallow seismic structure of young oceanic crust, *J. Geophys. Res.*, *92*(B9), 9351–9361.

Sempere, J. C., J. R. Cochran, and SEIR Scientific Team (1997), The Southeast Indian Ridge between 88°E and 120°E: Variations in crustal accretion at constant spreading rate, *J. Geophys. Res.*, *102*, 15,489–15,505.

Singh, S. C., W. C. Crawford, H. Carton, T. Seher, V. Combier, M. Cannat, J. P. Canales, D. Dusunur, J. Escartin, and J. M. Miranda (2006), Discovery of a magma chamber and faults beneath a Mid-Atlantic Ridge hydrothermal field, *Nature*, *442*, 1029–1032, doi:10.1038/nature05105.

Small, C. (1994), A global analysis of mid-ocean ridge axial topography, *Geophys. J. Int.*, *116*, 64–84, doi:10.1111/j.1365-246X.1994.tb02128.x.

Small, C., and D. T. Sandwell (1989), An abrupt change in ridge axis gravity with spreading rate, *J. Geophys. Res.*, *94*, 17,383–17,392.

Stewart, M. A., E. M. Klein, and J. A. Karson (2002), Geochemistry of dikes and lavas from the north wall of the Hess Deep Rift: Insights into the four-dimensional character of crustal construction at fast spreading mid-ocean ridges, *J. Geophys. Res.*, *107*(B10), 2238, doi:10.1029/2001JB000545.

Toksoz, M. N., C. H. Cheng, and A. Timur (1976), Velocities of seismic-waves in porous rocks, *Geophysics*, *41*, 621–645, doi:10.1190/1.1440639.

Tolstoy, M., F. Waldhauser, D. R. Bohnenstiehl, R. T. Weekly, and W.-Y. Kim (2008), Seismic identification of along-axis hydrothermal flow on the East Pacific Rise, *Nature*, *451*, 181–184, doi:10.1038/nature06424.

Van Ark, E. M., R. S. Detrick, J. P. Canales, S. M. Carbotte, A. J. Harding, G. M. Kent, M. R. Nedimovic, W. S. D. Wilcock, J. B. Diebold, and J. M. Babcock (2007), Seismic structure of the Endeavour Segment, Juan de Fuca Ridge: Correlations with seismicity and hydrothermal activity, *J. Geophys. Res.*, *112*, B02401, doi:10.1029/2005JB004210.

Vera, E. E., and J. B. Diebold (1994), Seismic imaging of layer 2A between 9°30′N and 10°N on the East Pacific Rise from two-ship wide-aperture profiles, *J. Geophys. Res.*, *99*, 3031–3041, doi:10.1029/93JB02107.

Vera, E. E., J. C. Mutter, P. Buhl, J. A. Orcutt, A. J. Harding, M. E. Kappus, R. S. Detrick, and T. M. Brocher (1990), The structure of 0- to 0.2-m.y.-old oceanic crust at 9°N on the East Pacific Rise from expanded spread profiles, *J. Geophys. Res.*, *95*, 15,529–15,556.

Weissel, J. K., and D. E. Hayes (1974), The Australian Antarctic Discordance: New results and implications, *J. Geophys. Res.*, *79*, 2579–2587, doi:10.1029/JB079i017p02579.

Wessel, P., and W. H. F. Smith (1995), New version of the generic mapping tools released, *Eos Trans. AGU*, *76*(33), 329.

West, B. P., J.-C. Sempere, D. G. Pyle, J. Phipps Morgan, and D. M. Christie (1994), Evidence for variable upper mantle temperature and crustal thickness in and near the Australian-Antarctic Discordance, *Earth Planet. Sci. Lett.*, *128*, 135–153, doi:10.1016/0012-821X(94)90141-4.

West, B. P., W. S. D. Wilcock, and J.-C. Sempere (1997), Three-dimensional structure of asthenospheric flow beneath the Southeast Indian Ridge, *J. Geophys. Res.*, *102*, 7783–7802, doi:10.1029/96JB03895.

Wilcock, W. S. D., S. C. Solomon, G. M. Purdy, and D. R. Toomey (1992), The seismic attenuation structure of a fast-spreading mid-ocean ridge, *Science*, *258*, 1470–1474, doi:10.1126/science.258.5087.1470.

Wilkens, R. H., G. J. Fryer, and J. Karsten (1991), Evolution of porosity and seismic structure of upper oceanic crust: Importance of aspect ratios, *J. Geophys. Res.*, *96*, 17,981–17,995, doi:10.1029/91JB01454.